

1 **Title:** EMT-derived alterations in glutamine metabolism sensitize mesenchymal breast cells
2 to mTOR inhibition

3

4 **Running title:** EMT-induced drug sensitivity in breast tissue

5

6 **Authors:**

7 Sigurdur Trausti Karvelsson¹, Arnar Sigurdsson², Kotryna Seip³, Maria Tunset Grinde⁴, Qiong
8 Wang¹, Freyr Johannsson¹, Gunhild Mari Mælandsmo³, Siver Andreas Moestue^{5,6}, Ottar
9 Rolfsson^{1*} & Skarphedinn Halldorsson^{1,7}

10

11 **Author affiliations:**

12 1. Center for Systems Biology, University of Iceland, Reykjavik, Iceland

13 2. Department of Chemistry, Technische Universität Berlin, Berlin, Germany

14 3. Department of Tumor Biology, Institute for Cancer Research, Oslo University Hospital,
15 Oslo, Norway

16 4. Department of Circulation and Medical Imaging, NTNU, Trondheim, Norway

17 5. Department of Clinical and Molecular Medicine, NTNU, Trondheim, Norway

18 6. Department of Pharmacy, Nord University, Namsos, Norway

19 7. Institute for Surgical Research, Vilhelm Magnus Laboratory, Oslo University Hospital, Oslo,
20 Norway

21 * Corresponding author

22

23 **Corresponding author information:**

24 Name: Óttar Rolfsson.

25 Mailing address: Sturlugata 8, 101 Reykjavik, Iceland.

26 Email address: ottarr@hi.is.

27 Phone number: 00354-8450075

28

29 **Conflict of interest:**

30 The authors declare no conflicts of interest.

31 **Abstract**

32 Epithelial-to-mesenchymal transition (EMT) is a fundamental developmental process with
33 strong implications in cancer progression. Understanding the metabolic alterations
34 associated with EMT may open new avenues of treatment and prevention. Here, we used ¹³C
35 carbon analogs of glucose and glutamine to examine differences in their utilization within
36 central carbon and lipid metabolism following EMT in breast epithelial cell lines. We found
37 that there are inherent differences in metabolic profiles before and after EMT. We observed
38 EMT-dependent re-routing of the TCA-cycle, characterized by increased mitochondrial IDH2 -
39 mediated reductive carboxylation of glutamine to lipid biosynthesis with a concomitant
40 lowering of glycolytic rates and glutamine-dependent glutathione (GSH) generation. Using
41 weighted correlation network analysis, we identified cancer drugs whose efficacy against the
42 NCI-60 Human Tumor Cell Line panel is significantly associated with GSH abundance and
43 confirmed these *in vitro*. We report that EMT-linked alterations in GSH synthesis modulate
44 the sensitivity of breast epithelial cells to mTOR inhibitors.

45 **Implications:** EMT in breast cells causes an increased demand for glutamine for fatty acid
46 biosynthesis, altering its contribution to glutathione biosynthesis which sensitizes the cells to
47 mTOR inhibitors.

48

49 **1. Introduction**

50 Epithelial-to-mesenchymal transition (EMT) is a fundamental developmental process where
51 tightly bound epithelial cells differentiate into migratory mesenchymal cells that can relocate
52 into adjacent or distant tissues. This process is vital for tissue restructuring during embryonic
53 development and is also necessary for proper wound healing in adult tissue. EMT has strong
54 implications in cancer progression and metastasis where primary tumor cells of epithelial
55 origin can take on a motile phenotype with the ability to migrate through the body and
56 establish secondary tumors at distant locations ¹.

57 Metabolic reprogramming is recognized as one of the ten cancer hallmarks as proposed by
58 Hanahan and Weinberg ². In contrast to rapidly dividing cancer cells, a mesenchymal
59 phenotype faces a different set of metabolic requirements whose relation to malignant

60 transformation has been intensely studied and associated with enhanced glycolysis,
61 increased glutaminolysis, nucleotide metabolism and abnormal choline metabolism³⁻⁵.
62 Quantitative understanding of the metabolic requirements of mesenchymal cells is however
63 lacking, particularly the changes to the turnover and quantity of metabolites involved in
64 xenobiotic clearance, *i.e.* the drug response of cells. Cancer cells that undergo EMT have
65 increased resistance to various drugs⁶⁻⁸, which indicates that the xenobiotic clearance of the
66 cells is altered. There are three phases involved in the metabolism of xenobiotics: I)
67 Modification, II) Conjugation and III) Excretion. Conjugation involves the binding of particular
68 metabolites (*e.g.* glutathione, UDP-glucuronate, PAPS, S-adenosylmethionine) to a
69 xenobiotic compound⁹, which leads to the assumption that the availability of these
70 metabolites within cells influences the activity of the drugs. Therefore, accurate metabolic
71 measurements of EMT may contribute to better understanding of the drug resistance of
72 cancer cells and lead to novel therapeutic approaches aimed at eliminating metastatic
73 cancer cells.

74 We have previously used both ultra-performance liquid chromatography coupled mass
75 spectrometry (UPLC-MS) and NMR to study EMT and cancer metabolism¹⁰⁻¹². Integrated
76 analyses of these metabolomics data with transcriptomic and proteomic data within
77 genome-scale metabolic models predicted metabolic differences that occur following EMT in
78 breast epithelium¹². These included alterations to glycolysis, the pentose phosphate
79 pathway, TCA cycle and fatty acid synthesis. Although these models provided useful insights
80 into metabolic alterations associated with EMT, they lacked accuracy in predicting internal
81 fluxes in a quantitative manner in the compartmentalized central carbon metabolism.

82 In order to better understand the metabolic changes that accompany EMT we characterized
83 the internal flow of metabolites in D492 breast epithelial cells and their mesenchymal
84 variant, D492M, to determine metabolic changes within central carbon metabolism
85 following EMT in breast epithelial cells. We performed stable isotope tracing of ¹³C labeled
86 glucose and two separate ¹³C labeled glutamine analogs. UPLC-MS and NMR were used to
87 measure label incorporation into metabolites associated with central carbon metabolism
88 and lipid biosynthesis. We subsequently performed shRNA lentiviral silencing of key genes to
89 further elucidate their role in EMT metabolic re-programming. Finally, using an integrated
90 network analysis of the NCI-60 Human Tumor Cell Line panel and an untargeted

91 metabolomic analysis, we investigate how the EMT-dependent re-routing of central carbon
92 metabolism affects drug responsiveness in D492 and D492M cells.

93

94 **2. Materials and methods**

95 **2.1 Cell culture**

96 D492 and D492M cells were kindly provided by the Stem Cell Research Unit, University of
97 Iceland, and were cultured in DMEM/F12-based medium H14 at 37°C in 5% CO₂ as
98 previously described¹³. All experiments were performed within 4 passages from thawing,
99 within the range of 30-40 passages in total. For the labeling experiments, the cells were fed
100 with medium containing 100% ¹³C-labeled glutamine at the 1 or 5 position (Cambridge
101 Isotope Laboratories, Inc., MA, USA) or ¹³C-labeled glucose at the 1 and 2 positions
102 (Cambridge Isotope Laboratories, Inc.). Cells were screened for *Mycoplasma* infections every
103 month using PCR-based tests at the Biomedical Center, University of Iceland.

104

105 **2.2 Lentiviral shRNA production and transduction**

106 HEK293T cells were transfected using TurboFect transfection reagent (Thermo Fisher
107 Scientific, MA, USA) at 80% confluency in T25 cell culture vessels. The cells were then
108 incubated at 37°C and 5% CO₂. Viral supernatant was collected at two timepoints, the first
109 being after 48 hours in culture, and the second 72 hours after changing medium at the first
110 timepoint. The viral supernatant was filtered through a 0.45 µm filter using a syringe and
111 stored at -20°C until usage. The lentiviral vectors were acquired from GeneCopoeia. They
112 contained an shRNA construct for the selective targeting of IDH2. The construct was based
113 on a psi-LVRH1MH vector with an mCherry fluorescent reporter, resistance against
114 hygromycin B and the identical hairpin sequence TCAAGAG. The target sequence was IDH2
115 5'GTACAAGGCCACAGACTTTGT-3'. The D492 and D492M cell lines were transduced using 1
116 mL of filtered viral supernatant at 70% confluency and incubated at 37°C and 5% CO₂ for 24
117 hours, at which timepoint the medium was changed to fresh H14 medium. After further 48
118 hours, the cells were grown in medium containing hygromycin B (200 µg/mL) for three
119 weeks to selectively grow cells containing the shRNA construct.

120

121 **2.3 Real-Time PCR**

122 Whole-cell RNA was extracted using Tri-Reagent (Thermo Fisher Scientific, AM9738). Reverse
123 transcription was performed using High-Capacity cDNA Reverse Transcription kit (Thermo
124 Fisher, 4368814). The expression of the genes *IDH1* and *IDH2* was quantified, where *ACTB*
125 (*Beta-actin*) and was used as an endogenous reference gene. The primers for *IDH1*, *IDH2* and
126 *ACTB* were designed using the Primer3 software in the Benchling website
127 (<https://benchling.com>). Primers were designed to span exon junctions and have a melting
128 temperature above 55°C. The expression of *IDH2* and *IDH1* was assessed using real-time PCR
129 (qPCR). Real-time quantitative PCR reactions were carried out using Luna[®] Universal qPCR
130 Master Mix (New England Biolabs, MA, USA) according to manufacturer's instructions on a
131 Bio-Rad CFX384 Touch™ Real Time System (Bio-Rad, CA, USA). Gene expression levels were
132 determined using CFX Manager Software (Bio-Rad) and differences in relative expression
133 were estimated with the $2^{\Delta\Delta Ct}$ method. The primer sequences used for quantifying the gene
134 expression were: *IDH1*-forward 5'-CGACATGGTGGCCCAAGCTATG-3', *IDH1*-reverse 5'-
135 TCATGCCGAGAGAGCCATACCC-3', *IDH2*-forward 5'-ATGAGGCCCGTGTGGAAGAGTT-3', *IDH2*-
136 reverse 5'-CAGATGATGGGCTCCCGGAAGA-3', *ACTB*-forward 5'-
137 CTCCTGGGTGAGTGGAGACTG-3' and *ACTB*-reverse 5'-GAGGGAAATGAGGGCAGGACTT-3'.

138

139 **2.4 Proliferation assay**

140 Cells were seeded in quadruplicates in 48-well plates (10.000 cells/well). They were grown in
141 a large chamber incubation system (PeCon GmbH, Erbach, Germany) at 37°C in 5% CO₂ and
142 imaged for 12-72 hours using Leica DMI6000B. Images of cells were opened with Fiji¹⁴,
143 where the cells were counted with the help of an in-house script.

144

145 **2.5 Detection of intracellular NADP⁺ and NADPH**

146 NADP⁺ and NADPH were measured using NADP/NADPH-Glo™ Assay (G9081, Promega,
147 Madison, WI). Cells were seeded in triplicates in opaque 96-well plates (10.000 cells/well)
148 and incubated at 37°C in 5% CO₂. After 24 hours, the medium was removed, cells were

149 washed with cold PBS and then supplemented with 50 μ L PBS and 50 μ L 1% DTAB in 0.2N
150 NaOH solution to induce cell lysis. Next steps were according to manufacturer's protocol.
151 The luminescence was measured 50 minutes after addition of the NADP-NADPH-Glo™
152 Detection reagent in SpectraMax® M3 Microplate Reader (Molecular Devices, CA, USA).

153

154 **2.6 Nuclear magnetic resonance (NMR)**

155 For NMR analysis, D492 and D492M cells were cultured in T225 flasks in supplemented
156 DMEM/F12 until they reached approximately 70% confluency. Cells were then fed with
157 either 1,2-¹³C glucose or 1-¹³C glutamine for 6 hours. Parallels without ¹³C tracers were also
158 cultured. Culture medium was collected after incubation. Methanol extracts from glucose-
159 and glutamine-labeled cells were prepared as described previously ¹⁵. The cell extracts were
160 freeze dried prior to NMR analysis. For NMR, freeze-dried cell extracts were dissolved in 600
161 μ L D₂O in PBS while culture medium (500 μ L) was diluted with in D₂O-based PBS (100 μ L).
162 NMR analysis was performed using a 600 MHz Bruker Avance III NMR spectrometer (Bruker
163 Biospin GmbH, Germany), equipped with a 5 mm QCI Cryoprobe with integrated, cooled
164 preamplifiers for ¹H, ²H and ¹³C. Proton spectra were acquired at 300 K using 1D NOESY
165 (Bruker: noesygppr1d) with presaturation and spoiler gradients as previously described ¹⁶.
166 The spectra were collected with 32 scans and 4 dummy scans. The acquisition time was 2.73
167 s and relaxation delay 4 s, measuring the FID via collection of 64 K complex data points. The
168 ¹H spectra were Fourier transformed with a 0.3 Hz exponential line broadening and the
169 chemical shift was calibrated to alanine at 1.48 ppm. ¹H spectra from D492 (n=5) and D492M
170 (n=6) cells were transferred to MATLAB R2017a for multivariate data analysis. The spectra
171 were baseline corrected using asymmetric least squares method ¹⁷ and peak aligned using
172 icoshift ¹⁸. The water peak and areas in the spectra with contamination and noise only were
173 removed. All spectra were mean normalized and mean centered. Principal component
174 analysis (PCA) was performed using PLS toolbox v8.2.1 (Eigenvector Research, WA, USA).
175 Proton decoupled ¹³C spectra (Bruker: zgpg30) were acquired using a power gated
176 decoupling sequence with a 30° pulse angle as described in Bettum *et al.* ¹⁹. The spectra
177 were collected with either 4 K (for 1,2-¹³C-glucose) or 16 K (for 1-¹³C-glutamine) scans and 16
178 dummy scans. The acquisition time was 1.65 s, relaxation delay 0.5 s, measuring the FID via
179 collection of 96 K complex data points over a sweep width of 197.175 ppm. The ¹³C spectra

180 were Fourier transformed with a 3.0 Hz exponential line broadening and the chemical shift
181 was calibrated to the 3-¹³C-alanine peak at 19.0 ppm or 1-¹³C-glutamine peak at 176.4 ppm.
182 ¹³C-labeled metabolites downstream from the tracers were identified by comparing ¹³C
183 spectra with natural abundance spectra acquired under the same conditions. Levels of
184 selected metabolites in the extracts were semi-quantitatively assessed by integration of
185 resonance signals using TopSpin 4.0.8 (Bruker Biospin GmbH) after correcting for natural
186 abundance levels. The ¹³C spectra were normalized to the total area under the curve (AUC)
187 in the ¹H spectra acquired from the same sample.

188

189 **2.7 Metabolomics**

190 *2.7.1 Sample extraction*

191 Polar and non-polar metabolites were extracted from cell cultures by
192 methanol/chloroform/water extraction. Cells were harvested in ice-cold methanol, vortexed
193 vigorously and let stand on ice for 10 minutes. Equal amounts of water and chloroform were
194 added to a final composition of 1:1:1 (CH₃OH:H₂O:CHCl₃), vortexed and left to stand
195 overnight at 4°C. The organic phase (lipids) was collected into a glass vial and dried in a
196 stream of N₂ and stored under N₂ at -80°C until analysis. The aqueous phase (polar
197 metabolites) was stored at -80°C and evaporated in a miVac concentrator (SP Scientific,
198 Warminster PA, USA) before analysis.

199 *2.7.2 UPLC-MS*

200 Before UPLC-MS analysis, the organic phase was reconstituted in MTBE before a methanol
201 solution containing 1M NaOH was added (10:1 v/v, respectively). This was incubated for 3.5
202 hours at 37°C, when 1 µL formic acid was added (to neutralize the solution), the samples
203 were dried in a stream of N₂ and then resuspended in isopropanol:ACN:H₂O (6:9:1, v/v/v).
204 The aqueous phase (metabolites) were reconstituted in isopropanol:ACN:H₂O (2:1:1, v/v/v).
205 Ultra performance liquid chromatography (UPLC) (Acquity, Waters, Manchester, UK) was
206 coupled with a quadrupole-time of flight mass spectrometer (Synapt G2, Waters,
207 Manchester, UK). For the lipid samples, chromatographic separation was achieved as
208 previously described ²⁰. For the metabolomic samples, chromatographic separation was
209 achieved by hydrophilic interaction liquid chromatography (HILIC) using an Acquity amide

210 column, 1.7 μm (2.1 x 150 mm) (Waters, Manchester, UK). All samples were analyzed in
211 positive ionization and negative ionization mode using acidic and basic chromatographic
212 conditions. In positive mode and in negative acidic conditions, mobile phase A was 100%
213 ACN and B was 100% H₂O both containing 0.1% formic acid. The following elution gradient
214 was used: 0 min 99% A; 7 min 30% A; 7.1 min 99% A; 10 min 99% A. In negative mode basic
215 conditions, mobile phase A contained ACN:sodium bicarbonate 10 mM (95:5) and mobile
216 phase B contained ACN:sodium bicarbonate 10 mM (5:95). The following elution gradient
217 was used: 0 min 99% A; 6 min 30% A; 6.5 min 99% A; 10 min 99% A. In all conditions, the
218 flow rate was 0.4 mL/min, the column temperature was 45°C, and the injection volume was
219 3.5 μL . The mass spectrometer was operated using a capillary voltage of 1.5 kV, the sampling
220 cone and the extraction cone were of 30 V and 5 V. The cone and the desolvation gas flow
221 were 50 L/h and 800 L/h, while the source and desolvation gas temperature were 120°C and
222 500°C. MS spectra were acquired in centroid mode from m/z 50 to 1000 using scan time of
223 0.3 s. Leucine enkephalin (2 ng/ μL) was used as lock mass (m/z 556.2771 and 554.2615 in
224 positive and negative experiments respectively). A typical analytical block consisted of: 1)
225 pooled QC samples to equilibrate the system, 2) calibrators, 3) samples and spiked pooled
226 QC samples and 4) calibrators.

227 2.7.3 Data analysis

228 TargetLynx (v4.1; Waters) was used to integrate chromatograms of all isotopologues of the
229 metabolites of interest. Ion chromatograms were extracted using a window of 0.02 mDa
230 which was centered on the expected m/z for each targeted isotopologue. The output was a
231 mass distribution vector (MDV) describing the relative amount of each detected
232 isotopologue of the metabolite. Ion chromatograms of isotopologues of interest extracted
233 and corrected for abundance of naturally occurring isotopes using the IsoCor software²¹.
234 When calculating the total contribution (TC) of carbon sources to metabolites, we used the
235 following equation²² :

$$TC = \frac{\sum_{i=0}^n i \cdot m_i}{n} \quad (1)$$

236 Where n is the number of C atoms in the metabolite, i represents the isotopologues and m is
237 the relative fraction of the isotopologues.

238 In order to evaluate the percentage of glucose that enters the oxidative part of the pentose
239 phosphate pathway, and re-enters glycolysis, we utilized a formula from Lee *et al.*²³:

$$PPP_{cycle} = \frac{m1/m2}{3 + m1/m2} \quad (2)$$

240 In equation 2, m1 and m2 are the fractional abundances of M+1 and M+2 lactate
241 isotopologues, respectively, (*e.g.* from **Figure S2**).

242

243 **2.8 RNA sequencing**

244 Quantified transcript pseudocounts from kallisto²⁴ were obtained for D492 and D492M in
245 triplicates from Briem *et al.* (from the authors)²⁵. These data were imported into R and
246 simultaneously log2-transformed and variance-stabilized using DESeq2's rlog function²⁶.

247

248 **2.9 Proteomic analysis**

249 A proteomic dataset for the D492 and D492M cells was obtained from the ProteomeXchange
250 Consortium via the PRIDE²⁷ partner repository with the dataset identifier PXD024164. The
251 raw data were processed using MaxQuant²⁸ for both the protein identification and
252 quantification.

253

254 **2.10 Western blot analysis**

255 D492 and D492M cells were grown to 80-90% confluent as described above followed by lysis
256 in RIPA buffer. The lysates were subjected to five freeze-thaw cycles, centrifuged at 14000
257 RCF for 20 minutes at 4°C. Protein concentration was quantified using a Pierce BCA Protein
258 Assay kit (Thermo).

259 10-20 µg of protein were loaded onto pre-cast 4-12% NuPAGE Bis-Tris gels (Thermo) and
260 transferred to a 0.45 µm nitrocellulose membrane (Thermo). The membrane was blocked in
261 5% BSA (Thermo) for 60 minutes, followed by overnight primary antibody incubation at 4°C.
262 The primary antibody was anti-IDH2 monoclonal rabbit (12652, Cell Signaling Technologies,

263 MA, USA) in 1:1000 dilution. IDH2 levels were normalized against β -actin (MA5-15739,
264 Thermo) in 1:10000 dilution.

265 Bands were detected by secondary antibody incubation for two hours at room temperature
266 using anti-rabbit IgG (H+L) DyLight™ 800 4x PEG Conjugate and anti-mouse IgG (H+L)
267 DyLight™ 680 Conjugate (Cell Signaling Technologies) in 1:15000 dilution. Imaging was
268 performed using Odyssey® CLx (LI-COR Biosciences, NE, USA) to scan the films at 169 μ m
269 resolution. The results were analysed in the Image Lab™ software (Bio-Rad).

270

271 **2.11 Measurement of metabolite exchange rates**

272 Glucose and lactate measurements were performed in an ABL 90 blood gas analyzer
273 (Radiometer, Brønshøj, Denmark). Glutamine uptake was measured using L-
274 Glutamine/Ammonia assay kit (K-GLNAM, Megazyme, Bray, Ireland). The following formula
275 was used to quantify the exchange rates of metabolites in the cells:

$$v_k = \frac{V([M_k]_f - [M_k]_i)}{A} \quad (3)$$

276 Where v_k is the exchange rate for metabolite k, $[M_k]_{48}$ and $[M_k]_0$ are the concentrations of
277 metabolite k in the culture media after 48 and 0 hours, respectively, and A is the area under
278 the growth curve.

279

280 **2.12 Weighted correlation network analysis**

281 Drug sensitivity data were gathered from the NCI-60 Human Tumor Cell Lines²⁹ using the
282 rcellminer R-package³⁰. We focused specifically on FDA-approved drugs so after filtering the
283 data (using WGCNA's goodSamplesGenes function³¹), the final size of the drug sensitivity
284 matrix was 214 drugs x 59 cell lines (one cell line, MDA-N, was removed due to missing
285 data). To construct a network of drug-sensitivities, a weighted correlation network analysis
286 was employed using the WGCNA R-package³¹. A soft threshold value of 9 was used to obtain
287 a scale-free network topology ($R^2 = 0.85$). Highly correlated modules that had an average
288 distance < 0.65 were merged. To associate the modules to a specific mechanism of action
289 (MOA), the MOA terms for each drug were obtained (from rcellminer) and tested for

290 overrepresentation in the modules. MOA with Bonferroni-adjusted p-value < 0.05 were
291 labeled as overrepresented and used for the functional annotation of the drug modules.
292 The eigenvalues (first principal components) for each module were identified and used to
293 test association of drug-modules with metabolite levels. The correlation of the drug modules
294 to metabolite levels of the cells within the NCI-60 (from Ortmayr *et al.* ³²) was calculated.
295 The R-package igraph ³³ was used to visualize the drug correlation network using the
296 Fruchterman-Reingold ³⁴ force-directed layout. An R-script for the network analysis is in
297 **Supplementary file 1.**

298

299 **2.13 Drug treatment assays**

300 Cells were seeded (3000 cells/well) in white Costar® 96-well plates (Corning, NY, USA) and
301 maintained at 37°C in 5% CO₂. After 24 hours, drugs were added with or without buthionine
302 sulphoximine (BSO; B2515, Sigma Aldrich) where DMSO was used as a control. Then, 72
303 hours later cell viability was evaluated using the CellTiter-Glo® (CTG) assay (Promega,
304 Madison, WI, USA), by adding CTG assay mix directly into the wells in a 1:1 ratio. After 10
305 minutes, luminescence was measured by Victor™ X3 Multiplate reader (Perkin Elmer, MA,
306 USA). The drugs tested were mTOR inhibitor everolimus (Sigma Aldrich) and taxane drug
307 paclitaxel (Fresenius Kabi, Halden, Norway).

308

309 **2.14 Detection of intracellular glutathione abundance**

310 Cells were seeded (2000 cells/well) in white 384-well plates (Greiner Bio-One,
311 Kremsmünster, Austria) and maintained at 37°C in 5% CO₂. After 24 hours, BSO (treated) or
312 medium (non-treated) was added. After additional 24 (and 48 for non-treated) hours,
313 glutathione measurement was performed by using GSH-Glo Glutathione Assay kit (V6911,
314 Promega) in accordance with the manufacturer's protocol.

315

316 **2.15 Statistical analysis**

317 Student's t-test was employed for comparison of two treatments. Benjamini-Hochberg
318 adjustment for multiple comparisons was performed when appropriate. Analysis of variance
319 (ANOVA) was used to compare data from three or more treatments or the simultaneous
320 evaluation of the effect of two grouping variables. The asterisks in each figure represent the
321 p-values (* < 0.05, ** < 0.01, *** < 0.001, **** < 0.0001, ns = not significant). Data were
322 assumed to be normally distributed. Statistical analysis and image generation was carried
323 out in the R environment ³⁵ using the *ggplot2* ³⁶ and *ggpubr* ³⁷ packages. In our graphs, all
324 data points are plotted and summarized using mean and standard error.

325

326 **3. Results**

327 **3.1 Glycolysis rates determine the pentose phosphate shunt in the D492 EMT cell model**

328 A clear difference in the overall metabolic profiles of D492 and D492M cells was confirmed
329 by principal component analysis (PCA) of their 1H NMR spectra. The score and loading plots
330 from PCA (**Figures S1A** and **S1B**) indicated that D492 cells had more intracellular isoleucine,
331 leucine, valine, alanine, arginine, glutathione, myo-inositol, asparagine, proline, AMP, ADP,
332 ATP, tyrosine, phenylalanine, and NAD⁺, and less glutamine, glutamate, phosphocholine,
333 glycine, threonine, glucose, fumarate, NADP and NADH. The rate of glucose uptake and
334 lactate secretion was also higher in the epithelial phenotype of D492 cells compared to the
335 mesenchymal phenotype (**Figure 1B**), indicative of enhanced glycolysis in D492. To
336 determine pentose phosphate pathway (PPP) split ratios in the cell lines we used 1,2-¹³C
337 glucose (**Figure 1A**) as previously described ³⁸. Label contribution of 1,2-¹³C-glucose to
338 lactate after 6 hours was higher in D492 epithelial cells than in D492M mesenchymal cells
339 (**Figure 1C**) confirming enhanced glycolysis. In order to determine the differences in PPP
340 activity we calculated the percentage of glucose diverted into the PPP using measured
341 lactate isotopologue abundances (**Figure S2**) and equation 2. Roughly 2% of glucose was
342 found to enter the PPP cycle in both cell lines. Therefore, because of the overall higher
343 glucose uptake, the flux into oxidative PPP is higher in D492. As a result, reduction of NADP
344 to NADPH via the oxidative phase of the PPP in D492M cells is dampened.

345 To examine the contribution of glucose to the TCA cycle, we measured the contribution of
346 the labeled 1,2-¹³C-glucose to citrate. Citrate is either oxidized for energy production in the

347 TCA cycle or used as a precursor for lipid biosynthesis³⁹ through ATP-citrate lyase (ACLY) in
348 the cytosol (**Figure 1A**). No difference in glucose-dependent citrate generation (**Figure 1D**)
349 was observed which was reflected by the contribution of glucose to palmitate (**Figure 1E**).
350 Furthermore, the contribution of glucose to other TCA cycle components and downstream
351 metabolites (malate, aspartate and glutamate) after 6 hours in culture was minimal (**Figure**
352 **S2**). Thus, the only difference in glucose utilization within central carbon metabolism
353 between D492 and D492M was the increased glycolytic activity of the former.

354

355 **3.2 Glutamine fuels citrate and lipogenic acetyl-CoA production via reductive carboxylation** 356 **following EMT in D492 cells**

357 Glutamine is a major contributor of carbons into the TCA cycle through anaplerosis (*i.e.*
358 glutaminolysis), particularly in cancer cells^{40–42}. Glutamine is the second-highest consumed
359 carbon source in D492 and D492M (after glucose¹²) with an average uptake rate of around
360 60 fmoles/cell/hour in both cell lines (**Figure 2B**). We found that both glucose and glutamine
361 are essential for the proliferation of D492 and D492M (**Figure S3**). Glutamine can replenish
362 the TCA cycle via glutamate and α -ketoglutarate which can be metabolized within the TCA
363 cycle both oxidatively and reductively (**Figure 2A**). In order to discriminate oxidative and
364 reductive TCA cycle carbon flow, D492 and D492M cells were cultured with isotopic
365 glutamine analogs labeled at either the 1 or 5 positions. These isotopomers of glutamine
366 allow the specific quantification of glutamine to citrate either reductively (1-¹³C-glutamine)
367 or oxidatively (5-¹³C-glutamine) (**Figure 2A**). The 5-¹³C-glutamine analog can additionally
368 quantify the contribution of glutamine to fatty acids solely through reductive carboxylation
369 (**Figure 2A**). Importantly, intracellular glutamate label from a labeled glutamine source is a
370 direct measurement of the contribution of glutamine to the glutamate pool. Compared to
371 D492, the glutamate pool in the D492M cells was not as dependent on glutamine as
372 observed from lower labeling incorporation from both 1- and 5-¹³C glutamine (**Figures S4A**
373 **and B**). This was supported by NMR measurements (**Figure S1C**) and is likely due to higher
374 amounts of glutamate being derived from elsewhere (*e.g.* transamination reactions and
375 protein catabolism) in D492M. As we were specifically interested in the contribution of
376 glutamine to metabolites beyond glutamate (*e.g.* citrate), we accounted for the differences
377 in glutamine-to-glutamate labeling by dividing the total contribution from glutamine to the

378 target metabolites with the total contribution of glutamine to glutamate in each cell line.
379 The results therefore represent the relative contribution of glutamate to metabolites.

380 Approximately 60% of the citrate pool was derived from glutamate in both D492 and D492M
381 as shown by the isotope enrichment from 5-¹³C glutamine (**Figure 2C**). Enrichment of ¹³C in
382 citrate derived from 1-¹³C glutamine was however higher in D492M (**Figure 2C**), supporting
383 increased reductive carboxylation. These results were mirrored in the 5-¹³C-glutamine-
384 dependent labeling profiles of palmitate, where there was a 6-fold increase in reductive
385 contribution of glutamine in D492M cells (**Figure 2D**).

386

387 **3.3 Metabolic re-routing following EMT affects redox metabolism in D492 cells**

388 The reductive pathway of glutamine to citrate is typically activated in hypoxia or following
389 changes in electron transport chain activity^{41,43,44}. Reductive glutaminolysis affects the redox
390 status of cells through NADPH which serves as a cofactor for the reversible isocitrate
391 dehydrogenase enzymes, IDH1 and IDH2⁴⁵. Interestingly, we observed an increased
392 NADPH/NADP ratio in D492M over D492 (**Figure 3A**) that is not compatible with the PPP
393 fluxes in the cells. However, even though reductive carboxylation is a NADPH-requiring
394 process (**Figure 3B**), studies have shown that its heightened activity may lead to increased
395 cytosolic or mitochondrial NADPH levels based on the coordination of different isoforms of
396 isocitrate dehydrogenase^{45,46}. NADPH is known for its role in defenses against reactive
397 oxygen species (ROS), where it is used to reduce the oxidized form of glutathione (GSSG) to
398 generate the reduced form of glutathione (GSH). Due to the observed alterations in
399 glycolysis, glutamine metabolism and NADPH/NADP⁺ ratios, we hypothesized that this would
400 be reflected in ROS generation within the cells. This in turn would translate to alterations in
401 glutathione metabolism.

402 Label incorporation from glutamine to glutathione was a significantly lower following EMT in
403 D492 cells as measured by UPLC-MS (**Figure 3C**) and NMR (**Figure S1C**), further supporting
404 EMT-associated alterations in redox metabolism. In addition, intracellular GSH concentration
405 was 33% lower in D492M cells on average (**Figure 3D**).

406 Proline has been shown to be important to maintain redox homeostasis, by recycling NADPH
407 to NADP⁺⁴⁷, coupling it to NADPH-generating pathways. Proline is synthesized from

408 glutamate in two reactions, both of which oxidize NADPH (**Figure 3E**). We traced the proline
409 synthesis from glutamate in D492 and D492M cells and observed a 2-fold increase in proline
410 synthesis from glutamate following EMT (**Figure 3F**). In summary, differences in the redox
411 state of the D492 EMT model can be related to decreased glycolytic/PPP flux and
412 concomitant changes to glutaminolysis that is defined by decreased GSH synthesis, increased
413 proline synthesis and increased reliance on reductive carboxylation for citrate synthesis.

414

415 **3.4 Mitochondrial isocitrate dehydrogenase 2 (IDH2) is essential for EMT-linked reductive** 416 **glutamine metabolism**

417 Based on the difference in reductive carboxylation and NADPH/NADP⁺ ratio (**Figure 2C** and
418 **3A**, respectively) and recent literature^{45,48}, we hypothesized that isocitrate dehydrogenase
419 (IDH) would contribute to the discrimination between the D492 and D492M metabolic
420 phenotypes (*i.e.* metabotypes) through glutamine consumption and influence redox balance.

421 Two isoforms of IDH are known to use NADP⁺ as a cofactor: Cytosolic IDH1 and
422 mitochondrial IDH2. Quantification of IDH mRNA (by RNA sequencing) and protein (by MS
423 proteomics) in D492 and D492M cells revealed increased IDH2 levels in D492M as compared
424 to D492 (**Figure 4A**). These findings were confirmed by Western blot (**Figure S5**). No
425 difference was observed in IDH1 levels (**Figure 4A**). Using shRNA lentiviral transduction, we
426 knocked down IDH2 expression in both cell lines and investigated the metabolic and
427 morphological effects.

428 Following a significant reduction in IDH2 expression levels, the mRNA levels of the cytosolic
429 isoform IDH1 did not change in the D492M-IDH2 cell line (**Figure 4B**). There were no
430 differences observed in neither morphology nor growth rate upon IDH2 knockdown in
431 D492M (**Figure 4C** and **D**). A significant reduction in reductive carboxylation activity was
432 observed, as indicated by the 1-¹³C-glutamine contribution to citrate and 5-¹³C-glutamine
433 contribution to palmitate (**Figure 4E** and **F**, respectively). No significant difference was
434 observed in the overall contribution of glutamine to citrate or glucose to citrate (**Figure 4E**).
435 The NADPH/NADP⁺ ratio was lowered upon IDH2 knockdown and proline synthesis from
436 glutamate was reduced (**Figure 4G** and **H**, respectively), suggesting that the redox
437 homeostasis of these cells is coupled to IDH2-mediated reductive carboxylation. The

438 glutamine-dependent synthesis of glutathione, however, was not affected by the IDH2
439 knockdown (**Figure 4I**). In contrast to D492M cells, D492 cells increased the expression of
440 the cytosolic isoform IDH1 upon IDH2 knockdown (**Figure S6A**). The upregulation of IDH1
441 was accompanied by increased glutamate-to-lipid contribution via reductive carboxylation
442 (**Figure S6B**) and decreased growth rate (**Figure S6C**). In addition, we observed a shift in
443 NADPH-to-NADP⁺ ratio, increased proline synthesis from glutamate and reduced glutathione
444 synthesis in the D492-IDH2 knock-down cells compared to the wildtype D492 cells (**Figure**
445 **S6D-F**). These results indicate that the epithelial phenotype, but not the mesenchymal
446 phenotype of D492 cells, can compensate for the IDH2 knockdown by increasing IDH1
447 expression.

448

449 **3.5 Alteration in glutathione biosynthesis drives sensitivity to mTOR inhibition**

450 The different metabolotypes of the cell lines, characterized by different glycolytic rates,
451 altered carbon source preference for TCA cycle activity and changes to the synthesis of
452 proline and glutathione are reminiscent of cancer stem cell metabolotypes^{49,50}. Due to
453 glutathione's role in drug resistance in various cancer cell types⁵¹⁻⁵³, we focused our
454 attention on the differences in glutathione metabolism between D492 and D492M cells
455 (**Figure 3**). We hypothesized that metabolic rerouting of glutamine-derived glutamate for
456 glutathione synthesis would affect drug sensitivity in these cells.

457 To identify drugs that are selectively affected by glutathione concentrations within cells, we
458 performed an integrated network analysis of 1) drug sensitivity profiles within the NCI-60
459 Human Tumor Cell Line database²⁹ and 2) untargeted metabolomic analysis of NCI-60 cell
460 lines from Ortmayr *et al.*³². The network analysis revealed that 214 FDA-approved drugs in
461 the NCI-60 database were grouped into 8 intra-correlated drug modules (**Figure 5A**), whose
462 functional annotation showed that drugs grouped together according to their mechanism of
463 action. The modules were comprised of DNA-damaging agents and cell cycle arresting
464 compounds (*e.g.* alkylating agents, nucleotide analogs, and paclitaxel, n = 122), hormones (n
465 = 7), tyrosine kinase inhibitors targeting EGFR and ERBB2 (*e.g.* erlotinib and lapatinib, n =
466 21), mTOR and serine/threonine kinase inhibitors (*e.g.* everolimus, rapamycin, temsirolimus,

467 n = 8), ALK/CDK inhibitors (n = 17), tyrosine kinases targeting VEGFR, PDGFR and FGFR (n =
468 7), MAP kinase inhibitors n = 10) and non-specific drugs (n = 6).

469 Interestingly, glutathione levels were negatively correlated with the mTOR inhibitor module,
470 represented in **Figure 5A** as the size of the nodes. When the modules were represented
471 collectively as a single unit using singular value decomposition, mTOR inhibitors were
472 significantly correlated with both reduced and oxidized glutathione (**Figure 5B**). This was
473 further supported by the Spearman correlation p-value for mTOR inhibitors and intracellular
474 GSH and GSSG levels (**Figure S7**). These results imply that high glutathione availability is
475 associated with low sensitivity to mTOR inhibitors and vice versa. Other conjugation
476 metabolites (*i.e.* UDP-glucuronate and S-adenosylmethionine) did not display this type of
477 relationship with mTOR inhibitors.

478 Following this we examined the effects of the mTOR inhibitor everolimus (strong negative
479 correlation with GSH levels) and paclitaxel (no correlation with GSH levels) on D492 and
480 D492M cells. D492M cells were more sensitive to both everolimus and paclitaxel than D492
481 (**Figure 5C**). In order to establish a functional link between glutathione abundance and mTOR
482 inhibitors, we co-treated D492 and D492M cells with buthionine sulfoximine (BSO), an
483 inhibitor of the rate-limiting enzyme glutamate-cysteine ligase (GCL) in glutathione synthesis
484 (**Figure 5D and E**), and either everolimus (**Figure 5F**) or paclitaxel (**Figure 5G**). The sensitivity
485 of both D492 and D492M cells to everolimus was enhanced by co-treatment with BSO,
486 whereas these effects were not observed when the cells were co-treated with paclitaxel and
487 BSO. Together, these data suggest that glutathione availability directly affects sensitivity to
488 drugs that specifically affect the mTOR pathway.

489

490 **4. Discussion**

491 D492 and D492M cells represent only two of the numerous phenotypes within the spectrum
492 of EMT⁵⁴. Herein, we have thoroughly characterized the central carbon metabolic activity of
493 these cell types using ¹³C isotope tracers, specialized metabolic assays, and shRNA-mediated
494 knockdown of gene expression. Furthermore, we have evaluated the functional
495 consequences of EMT-mediated differences in redox metabolism using both *in silico* and *in*
496 *vitro* drug-sensitivity analyses.

497

498 **4.1 IDH2 plays a key role in EMT in breast epithelium**

499 The data presented here support previous findings where genome-scale metabolic models¹²
500 and signal-network models constrained with cell type-specific transcriptomic data⁵³
501 predicted lower glycolytic activity of D492M cells compared to D492 cells. In addition, the
502 data indicate that D492M cells increasingly rely on reductive carboxylation of glutamine to
503 citrate via isocitrate dehydrogenase activity. Transcriptomic and proteomic data from D492
504 and D492M cells confirm that the predominant EMT-associated form of isocitrate
505 dehydrogenase is the mitochondrial NADP⁺-dependent IDH2, with D492M cells showing
506 significantly higher levels on both the transcript and protein levels (**Figure 4A**). Knockdown
507 of IDH2 by lentiviral shRNA induction caused a marked reduction of reductive carboxylation
508 of glutamine to citrate in D492M cells but did not affect the overall contribution of either
509 glucose or glutamine to citrate (**Figure 4E**). These results were reflected in the label
510 incorporation of 5-¹³C-glutamine and 1,2-¹³C-glucose to palmitate (**Figure 4F**). The decrease
511 in citrate labeling from 1-¹³C-glutamine indicates that in these cells, reductive carboxylation
512 primarily takes place within the mitochondria, as opposed to in the cytosol via IDH1 activity.

513 The knockdown of IDH2 and the subsequent re-routing of glutamine metabolism
514 significantly diminished the ratio of NADPH to NADP⁺ and the synthesis of proline from
515 glutamate (**Figure 4G and H**), consistent with the relationship of reductive carboxylation and
516 proline synthesis to redox homeostasis^{45,55}. However, there was no clear connection of IDH2
517 to glutathione synthesis (**Figure 4I**).

518 Our findings highlight the importance of IDH2 in the increased reductive carboxylation
519 following EMT in breast epithelium. However, we cannot exclude the importance of IDH1 in
520 this context. It is reasonable to assume that when reductive carboxylation takes place in the
521 cytosol via IDH1, the resulting citrate is transported into the mitochondria where IDH2 takes
522 part in its ultimate oxidation as previously proposed⁴⁵. When IDH2 levels are diminished, the
523 activity of this pathway would inevitably be halted. Nevertheless, our results demonstrate
524 that IDH2 knockdown significantly affects the reductive carboxylation of glutamine to citrate
525 and ultimately fatty acids which establishes a functional role of IDH2 in this process. Thus,

526 not only are the D492 and D492M cells different in their the overall lipid composition ⁵⁶, but
527 also the origin of lipid carbons.

528

529 **4.2 Alterations in reductive carboxylation and redox metabolism follow EMT in breast**

530 Our results show that glutamine-derived citrate is utilized for fatty acid synthesis in the D492
531 cell model, but the reliance on this pathway is enhanced following EMT. We show that there
532 is a concurrent increase in NADPH/NADP⁺ ratio and proline synthesis along with a decrease
533 in glutathione synthesis (**Figure 3C-F**). It has previously been shown that anchorage-
534 independent growth relies on increased reductive carboxylation and subsequent mitigation
535 of mitochondrial ROS ⁴⁵. The role of proline in anchorage-independent growth has also been
536 demonstrated by showing that its degradation and cycling is higher in breast cancer cells
537 grown in 3D culture than in 2D ⁵⁵, which ultimately altered the NADPH/NADP⁺ balance.
538 Phang ⁵⁷ hypothesized that in cancer cells, proline is directed away from protein synthesis
539 and towards redox regulation, a pathway that proline has previously been shown to
540 participate in within mammalian cells ⁵⁸. More recently, it was shown that NADPH-
541 dependent proline synthesis and reductive carboxylation act as alternative bins for electrons
542 under hypoxic conditions when the electron transport chain is disabled. This way, electron
543 transfer may continue functioning in cancer cells to maintain their viability ⁵⁰. These
544 observations fit well with the decreased oxygen consumption rate in D492M mesenchymal
545 cells ¹², their shift towards higher overall NADPH (*c.f.* **Figure 3B**), increased reductive
546 carboxylation and higher proline synthesis. Furthermore, D492M cells display a concomitant
547 decrease in glutathione synthesis and intracellular abundance. Interestingly, Snail mediated
548 EMT induction in MCF7 breast cancer cells has previously been shown to result in
549 intracellular glutathione reduction and elevation of ROS ⁵⁹.

550

551 **4.3 Diminished glutathione abundance potentiates sensitivity to PI3K/Akt/mTOR inhibitors**

552 We have previously reported a reduction in oxidative phosphorylation following EMT in
553 D492 cells ¹². This causes a metabolic shift towards anaplerosis, an upregulation of pathways
554 receiving otherwise ETC-directed electrons (*i.e.* proline synthesis and reductive
555 carboxylation) ⁵⁰ and decreased glutamine-derived glutathione synthesis. Glutathione is the

556 most abundant nonprotein thiol in animal cells and it plays a crucial role in the conjugation
557 phase of xenobiotic metabolism. This leads to increased water-solubility of foreign
558 compounds (*e.g.* drugs or toxins) and their reduced efficacy^{60,61}.

559 Due to the reduction in glutathione synthesis and overall abundance in the mesenchymal
560 D492M cells compared to epithelial D492 cells (**Figure 3C and D**), we hypothesized that this
561 would result in altered drug sensitivity of the mesenchymal phenotype. Integrated network
562 analysis suggested that D492M cells are more sensitive to drugs that specifically target
563 mTOR (**Figure 5A and B**). Furthermore, the lack of a significant relationship between UDP-
564 glucuronate and S-adenosylmethionine, compounds known to partake in the conjugation to
565 xenobiotic compounds⁹, suggests that mTOR inhibitors are specifically affected by
566 glutathione availability. We tested the efficacy of everolimus, a well-known mTOR inhibitor,
567 and found that D492M cells were more sensitive than D492 cells (**Figure 5C**). Furthermore,
568 we showed that depleting intracellular glutathione levels via BSO treatment (**Figure 5E**)
569 increased the sensitivity to everolimus (**Figure 5F**). In contrast, BSO treatment did not affect
570 sensitivity to paclitaxel, a microtubule stabilizer and mitotic inhibitor (**Figure 5G**). These
571 results indicate that glutathione availability primarily affects the sensitivity to drugs that
572 target the mTOR pathway.

573 In recent years, studies have shown a direct relationship between the mTOR signaling
574 pathway and oxidative stress response^{62,63}. Furthermore, mTOR signaling has been shown to
575 be highly relevant in the EMT process and chemoresistance of ovarian cancer cells and
576 melanoma^{64,65}. Collectively, our results introduce a valuable mechanistic insight into the
577 altered drug sensitivity following EMT in breast epithelium and support previous findings
578 that glutathione depletion in combination with mTOR inhibitors may specifically target the
579 metastatic potential and/or stemness of cancer cells.

580

581 **4.4 Conclusions**

582 In summary, we have defined alterations in central carbon metabolism of a breast epithelial
583 cell model of EMT using ¹³C carbon tracing. We show that glutamine metabolism is re-routed
584 towards reductive carboxylation to fuel fatty acid synthesis following EMT due to activity of
585 the mitochondrial NADP⁺-dependent isocitrate dehydrogenase (IDH2). This leads to

586 decreased glutathione production and disrupted redox homeostasis within the cells.
587 Integrated network analysis of the NCI-60 Human Tumor Cell Line database revealed a
588 negative correlation between intracellular glutathione levels and sensitivity to mTOR
589 inhibitors, and by depleting intracellular glutathione levels in D492 and D492M cells, we
590 sensitized them to mTOR pathway inhibitors. Our results highlight a potential metabolic
591 weakness of low-glutathione, EMT-derived cells that may be exploited in anti-metastatic
592 treatment.

593

594 **References**

- 595 1. Chaffer, C. L., San Juan, B. P., Lim, E. & Weinberg, R. A. EMT, cell plasticity and metastasis.
596 *Cancer Metastasis Rev.* **35**, 645–654 (2016).
- 597 2. Hanahan, D. & Weinberg, R. A. Hallmarks of cancer: The next generation. *Cell* vol. 144 646–
598 674 (2011).
- 599 3. Lee, S. Y. *et al.* Dlx-2 and glutaminase upregulate epithelial-mesenchymal transition and
600 glycolytic switch. *Oncotarget* **7**, 7925–7939 (2016).
- 601 4. Shaul, Y. D. *et al.* Dihydropyrimidine accumulation is required for the epithelial-mesenchymal
602 transition. *Cell* **158**, 1094–1109 (2014).
- 603 5. Koch, K. *et al.* Reciprocal regulation of the cholinic phenotype and epithelialmesenchymal
604 transition in glioblastoma cells. *Oncotarget* **7**, 73414–73431 (2016).
- 605 6. Fischer, K. R. *et al.* Epithelial-to-mesenchymal transition is not required for lung metastasis
606 but contributes to chemoresistance. *Nature* **527**, 472–476 (2015).
- 607 7. Zheng, X. *et al.* Epithelial-to-mesenchymal transition is dispensable for metastasis but induces
608 chemoresistance in pancreatic cancer. *Nature* **527**, 525–530 (2015).
- 609 8. Williams, E. D., Gao, D., Redfern, A. & Thompson, E. W. Controversies around epithelial–
610 mesenchymal plasticity in cancer metastasis. *Nat. Rev. Cancer* **19**, 716–732 (2019).
- 611 9. Jancova, P., Anzenbacher, P. & Anzenbacherova, E. Phase II drug metabolizing enzymes.
612 *Biomed. Pap.* **154**, 103–116 (2010).
- 613 10. Jóhannsson, F. *et al.* Systems analysis of metabolism in platelet concentrates during storage in
614 platelet additive solution. *Biochem. J.* **475**, 2225–2240 (2018).

- 615 11. Grinde, M. T. *et al.* Biomarker Discovery Using NMR-Based Metabolomics of Tissue. in 243–
616 262 (Humana, New York, NY, 2019). doi:10.1007/978-1-4939-9690-2_15.
- 617 12. Halldorsson, S. *et al.* Metabolic re-wiring of isogenic breast epithelial cell lines following
618 epithelial to mesenchymal transition. *Cancer Lett.* **396**, 117–129 (2017).
- 619 13. Sigurdsson, V. *et al.* Endothelial induced EMT in breast epithelial cells with stem cell
620 properties. *PLoS One* **6**, (2011).
- 621 14. Schindelin, J. *et al.* Fiji: An open-source platform for biological-image analysis. *Nature*
622 *Methods* vol. 9 676–682 (2012).
- 623 15. Itkonen, H. M. *et al.* Inhibition of O-GlcNAc transferase activity reprograms prostate cancer
624 cell metabolism. *Oncotarget* **7**, 12464–12476 (2016).
- 625 16. Austdal, M. *et al.* Metabolomic biomarkers in serum and urine in women with preeclampsia.
626 *PLoS One* **9**, (2014).
- 627 17. Eilers, P. H. C. Parametric Time Warping. *Anal. Chem.* **76**, 404–411 (2004).
- 628 18. Savorani, F., Tomasi, G. & Engelsen, S. B. icoshift: A versatile tool for the rapid alignment of 1D
629 NMR spectra. *J. Magn. Reson.* **202**, 190–202 (2010).
- 630 19. Bettum, I. J. *et al.* Metabolic reprogramming supports the invasive phenotype in malignant
631 melanoma. *Cancer Lett.* **366**, 71–83 (2015).
- 632 20. Kotronoulas, A. *et al.* Wound healing grafts: Omega-3 fatty acid lipid content differentiates
633 the lipid profiles of acellular Atlantic cod skin from traditional dermal substitutes. *J. Tissue*
634 *Eng. Regen. Med.* **14**, 441–451 (2020).
- 635 21. Millard, P., Letisse, F., Sokol, S. & Portais, J. C. IsoCor: Correcting MS data in isotope labeling
636 experiments. *Bioinformatics* **28**, 1294–1296 (2012).
- 637 22. Buescher, J. M. *et al.* A roadmap for interpreting ¹³C metabolite labeling patterns from cells.
638 *Current Opinion in Biotechnology* vol. 34 189–201 (2015).
- 639 23. Lee, W. N. P. *et al.* Mass isotopomer study of the nonoxidative pathways of the pentose cycle
640 with [1,2-¹³C₂]glucose. *Am. J. Physiol. - Endocrinol. Metab.* **274**, (1998).
- 641 24. Bray, N. L., Pimentel, H., Melsted, P. & Pachter, L. Near-optimal probabilistic RNA-seq
642 quantification. *Nat. Biotechnol.* **34**, 525–527 (2016).
- 643 25. Briem, E. *et al.* MiR-203a is differentially expressed during branching morphogenesis and EMT

- 644 in breast progenitor cells and is a repressor of peroxidasin. *Mech. Dev.* **155**, 34–47 (2019).
- 645 26. Love, M. I., Huber, W. & Anders, S. Moderated estimation of fold change and dispersion for
646 RNA-seq data with DESeq2. *Genome Biol.* **15**, 550 (2014).
- 647 27. Perez-Riverol, Y. *et al.* The PRIDE database and related tools and resources in 2019: Improving
648 support for quantification data. *Nucleic Acids Res.* **47**, D442–D450 (2019).
- 649 28. Cox, J. & Mann, M. MaxQuant enables high peptide identification rates, individualized p.p.b.-
650 range mass accuracies and proteome-wide protein quantification. *Nat. Biotechnol.* **26**, 1367–
651 1372 (2008).
- 652 29. Shoemaker, R. H. The NCI60 human tumour cell line anticancer drug screen. in *Nature*
653 *Reviews Cancer* vol. 6 813–823 (Nature Publishing Group, 2006).
- 654 30. Luna, A. *et al.* Rcellminer: Exploring molecular profiles and drug response of the NCI-60 cell
655 lines in R. *Bioinformatics* **32**, 1272–1274 (2016).
- 656 31. Langfelder, P. & Horvath, S. WGCNA: An R package for weighted correlation network analysis.
657 *BMC Bioinformatics* **9**, 559 (2008).
- 658 32. Ortmayr, K., Dubuis, S. & Zampieri, M. Metabolic profiling of cancer cells reveals genome-wide
659 crosstalk between transcriptional regulators and metabolism. *Nat. Commun.* **10**, 1–13 (2019).
- 660 33. Csardi, G. & Nepusz, T. The igraph software package for complex network research.
661 *InterJournal Complex Sy*, 1695 (2006).
- 662 34. Fruchterman, T. M. J. & Reingold, E. M. Graph drawing by force-directed placement. *Softw.*
663 *Pract. Exp.* **21**, 1129–1164 (1991).
- 664 35. R Core Team. R: A Language and Environment for Statistical Computing. (2020).
- 665 36. Wickham, H. *ggplot2: Elegant Graphics for Data Analysis*. (Springer-Verlag New York, 2016).
- 666 37. Kassambara, A. *ggpubr: 'ggplot2' Based Publication Ready Plots*. (2020).
- 667 38. Metallo, C. M., Walther, J. L. & Stephanopoulos, G. Evaluation of ¹³C isotopic tracers for
668 metabolic flux analysis in mammalian cells. *J. Biotechnol.* (2009)
669 doi:10.1016/j.jbiotec.2009.07.010.
- 670 39. Watson, J. A. & Lowenstein, J. M. Citrate and the conversion of carbohydrate into fat. Fatty
671 acid synthesis by a combination of cytoplasm and mitochondria. *J. Biol. Chem.* **245**, 5993–
672 6002 (1970).

- 673 40. Gaglio, D. *et al.* Oncogenic K-Ras decouples glucose and glutamine metabolism to support
674 cancer cell growth. *Mol. Syst. Biol.* **7**, (2011).
- 675 41. Yang, C. *et al.* Glutamine oxidation maintains the TCA cycle and cell survival during impaired
676 mitochondrial pyruvate transport. *Mol. Cell* **56**, 414–424 (2014).
- 677 42. Yoo, H. C., Yu, Y. C., Sung, Y. & Han, J. M. Glutamine reliance in cell metabolism. *Experimental
678 and Molecular Medicine* vol. 52 1496–1516 (2020).
- 679 43. Mullen, A. R. *et al.* Reductive carboxylation supports growth in tumour cells with defective
680 mitochondria. *Nature* **481**, 385–388 (2012).
- 681 44. Metallo, C. M. *et al.* Reductive glutamine metabolism by IDH1 mediates lipogenesis under
682 hypoxia. *Nature* **481**, 380–384 (2012).
- 683 45. Jiang, L. *et al.* Reductive carboxylation supports redox homeostasis during anchorage-
684 independent growth. *Nature* **532**, 255–8 (2016).
- 685 46. Du, J. *et al.* Reductive carboxylation is a major metabolic pathway in the retinal pigment
686 epithelium. *Proc. Natl. Acad. Sci. U. S. A.* **113**, 14710–14715 (2016).
- 687 47. Liu, W., Hancock, C. N., Fischer, J. W., Harman, M. & Phang, J. M. Proline biosynthesis
688 augments tumor cell growth and aerobic glycolysis: Involvement of pyridine nucleotides. *Sci.
689 Rep.* **5**, (2015).
- 690 48. Smolková, K., Dvořák, A., Zelenka, J., Vitek, L. & Ježek, P. Reductive carboxylation and 2-
691 hydroxyglutarate formation by wild-type IDH2 in breast carcinoma cells. *Int. J. Biochem. Cell
692 Biol.* **65**, 125–133 (2015).
- 693 49. Aguilar, E. *et al.* Metabolic Reprogramming and Dependencies Associated with Epithelial
694 Cancer Stem Cells Independent of the Epithelial-Mesenchymal Transition Program. *Stem Cells*
695 **34**, 1163–1176 (2016).
- 696 50. Liu, M. *et al.* Inhibiting both proline biosynthesis and lipogenesis synergistically suppresses
697 tumor growth. *J. Exp. Med.* **217**, (2020).
- 698 51. Yang, C. H., Kuo, M. L., Chen, J. C. & Chen, Y. C. Arsenic trioxide sensitivity is associated with
699 low level of glutathione in cancer cells. *Br. J. Cancer* **81**, 796–799 (1999).
- 700 52. Rocha, C. R. R. *et al.* Glutathione depletion sensitizes cisplatin- and temozolomide-resistant
701 glioma cells in vitro and in vivo. *Cell Death Dis.* **5**, e1505–e1505 (2014).

- 702 53. Nunes, S. C. & Serpa, J. Glutathione in ovarian cancer: A double-edged sword. *International*
703 *Journal of Molecular Sciences* vol. 19 (2018).
- 704 54. Zhang, Y. & Weinberg, R. A. Epithelial-to-mesenchymal transition in cancer: complexity and
705 opportunities. *Front. Med.* **12**, 361–373 (2018).
- 706 55. Elia, I. *et al.* Proline metabolism supports metastasis formation and could be inhibited to
707 selectively target metastasizing cancer cells. *Nat. Commun.* **8**, 15267 (2017).
- 708 56. Eiriksson, F. F. *et al.* Altered plasmalogen content and fatty acid saturation following epithelial
709 to mesenchymal transition in breast epithelial cell lines. *Int. J. Biochem. Cell Biol.* **103**, 99–104
710 (2018).
- 711 57. Phang, J. M. Proline Metabolism in Cell Regulation and Cancer Biology: Recent Advances and
712 Hypotheses. *Antioxid. Redox Signal.* **30**, 635–649 (2019).
- 713 58. Krishnan, N., Dickman, M. B. & Becker, D. F. Proline modulates the intracellular redox
714 environment and protects mammalian cells against oxidative stress. *Free Radic. Biol. Med.* **44**,
715 671–81 (2008).
- 716 59. Mezencev, R., Matyunina, L. V., Jabbari, N. & McDonald, J. F. Snail-induced epithelial-to-
717 mesenchymal transition of MCF-7 breast cancer cells: systems analysis of molecular changes
718 and their effect on radiation and drug sensitivity. *BMC Cancer* **16**, 236 (2016).
- 719 60. Zhang, K., Mack, P. & Wong, K. P. Glutathione-related mechanisms in cellular resistance to
720 anticancer drugs (Review). *International Journal of Oncology* vol. 12 871–882 (1998).
- 721 61. Forman, H. J., Zhang, H. & Rinna, A. Glutathione: Overview of its protective roles,
722 measurement, and biosynthesis. *Molecular Aspects of Medicine* vol. 30 1–12 (2009).
- 723 62. Li, J. *et al.* MTORC1-driven tumor cells are highly sensitive to therapeutic targeting by
724 antagonists of oxidative stress. *Cancer Res.* **76**, 4816–4827 (2016).
- 725 63. Hambright, H. G., Meng, P., Kumar, A. P. & Ghosh, R. Inhibition of PI3K/AKT/mTOR axis
726 disrupts oxidative stress-mediated survival of melanoma cells. *Oncotarget* **6**, 7195–7208
727 (2015).
- 728 64. Deng, J. *et al.* Inhibition of PI3K/Akt/mTOR signaling pathway alleviates ovarian cancer
729 chemoresistance through reversing epithelial-mesenchymal transition and decreasing cancer
730 stem cell marker expression. *BMC Cancer* **19**, (2019).
- 731 65. Seip, K. *et al.* Fibroblast-induced switching to the mesenchymal-like phenotype and

732 PI3K/mTOR signaling protects melanoma cells from BRAF inhibitors. *Oncotarget* **7**, 19997–
733 20015 (2016).

734

735 **Figure legends**

736 **Figure 1. Glucose metabolism of D492 and D492M.** A) A schematic overview of label distribution
737 from 1,2-¹³C glucose into central carbon metabolism. An atom transition map of glucose metabolism
738 showing a part of the metabolic fates of 1,2-¹³C glucose within mammalian cells, where the ¹³C-
739 isotopes are shown in black. Dashed lines indicate more than one reaction between metabolites. B)
740 Measured glucose uptake and lactate secretion in D492 and D492M. Total contribution of glucose to
741 C) lactate, D) citrate and E) palmitate was measured after culturing of D492 and D492M with 1,2-¹³C-
742 glucose for 6 hours. Metabolites: f6p – fructose 6-phosphate, g3p – glyceraldehyde 3-phosphate, pyr
743 – pyruvate, co2 – carbon dioxide, accoa – acetyl CoA, oac – oxaloacetate, αkg – α-ketoglutarate, suc –
744 succinate, fum – fumarate, mal – malate, asp – aspartate. Enzymes: CS – citrate synthase, ACLY –
745 ATP-citrate lyase. Pathways: PPP – Pentose phosphate pathway.

746

747 **Figure 2. Glutamine metabolism of D492 and D492M.** A) Atom transition map of glutamine
748 metabolism showing the different metabolic fates of 1-¹³C glutamine (grey) and 5-¹³C glutamine
749 (black) within mammalian cells. Dashed lines indicate more than one reaction between metabolites.
750 B) Measured glutamine uptake in D492 and D492M. C) Contribution of 1- and 5-¹³C-glutamine to
751 citrate in D492 and D492M cells after 6 hours in culture. The total contribution of the glutamine
752 analogs to citrate was normalized to the different origins of glutamate in the cells (total contribution
753 of glutamine to glutamate). D) Total contribution of 5-¹³C-glutamine to palmitate after 6 hours in
754 culture, normalized to glutamate origin. Metabolites: co2 – carbon dioxide, accoa – acetyl CoA, oac –
755 oxaloacetate, αkg – α-ketoglutarate, suc – succinate, mal – malate, asp – aspartate. Enzymes: ME –
756 malic enzyme.

757

758 **Figure 3. Redox metabolism is altered following EMT of D492.** A) NADPH-to-NADP ratio in D492 and
759 D492M cells. B) A schematic showing the connection of mitochondrial and cytosolic reductive
760 carboxylation, and NADP⁺/NADPH balance. C) Total contribution of glutamate to oxidized glutathione
761 (GSSG) in D492 and D492M cells after 6 hours in culture. D) Measured abundance of glutathione
762 (GSH) in D492 and D492M after 24 and 48 hours in culture. A two-way ANOVA test revealed a
763 significant difference in GSH levels between the cells, independent of time. E) The two reactions
764 needed to convert glutamate into proline. Both reactions oxidize NADPH. P5CS: Delta-1-pyrroline-5-
765 carboxylate synthase, PYCR: Pyrroline-5-carboxylate reductase. F) Total contribution of glutamate to
766 proline in D492 and D492M cells after 6 hours in culture. The results from B and D are from the
767 combined analysis of 1- and 5-¹³C-glutamine results, since both ¹³C carbons are detected in the
768 proline and GSSG carbon skeletons.

769

770 **Figure 4. IDH2 mediates reductive carboxylation activity and is coupled to redox metabolism of**
771 **D492M.** A) Relative differences in gene expression and protein translation of IDH1 and IDH2 in D492
772 and D492M. The results are displayed as log-fold D492M/D492 ratio of abundance of IDH1/2

773 transcripts from RNA sequencing, and IDH1/2 protein from a proteomic analysis of D492 and D492M.
774 Results are depicted as mean + standard error (n=3). B) Real-Time PCR from D492, D492M and an
775 IDH2 -silenced D492M cell line showing the gene expression levels of IDH2 and IDH1. C) Phase-
776 contrast images of D492M-WT and D492M-IDH2 cells. D) Proliferation of D492M-WT and D492M-
777 IDH2 cell lines (mean + standard error, n=8). E) Effect of IDH2 silencing on the contribution of 1-¹³C-
778 glutamine, 5-¹³C-glutamine and 1,2-¹³C-glucose to citrate in D492M, where the former two were
779 normalized to glutamate origin. F) Effect of IDH2 silencing on the contribution of 5-¹³C-glutamine
780 (normalized to glutamate origin) and 1,2-¹³C-glucose to palmitate in D492M. G) Effect of IDH2
781 silencing on the NADPH/NADP⁺ ratio in D492M. H) Effect of IDH2 silencing on the contribution of 1-
782 ¹³C-glutamine to proline (normalized to glutamate origin). I) Effect of IDH2 silencing on the
783 contribution of 1-¹³C-glutamine and 5-¹³C-glutamine to oxidized glutathione (normalized to glutamate
784 origin). E,F,H and I) are from cells cultured with ¹³C-labeled carbon sources for 6 hours. Student's
785 two-tailed t-test (with Benjamini-Hochberg adjustment for multiple comparisons) was used to
786 estimate significance of results.

787

788 **Figure 5. Glutathione levels regulate sensitivity to mTOR inhibitors.** A) Network analysis of NCI-60
789 cell lines treated with various FDA-approved drugs (n =214) suggests the presence of 8 modules of
790 intra-correlated drugs. The efficacy of each individual drug was correlated with glutathione levels,
791 represented by node size. B) The correlation of drug modules' eigenvalues to reduced glutathione
792 (GSH), oxidized glutathione (GSSG), UDP-glucuronate and S-adenosylmethionine (SAM). Upper
793 numbers in table represent Pearson's correlation coefficient and the lower numbers (in brackets)
794 represent the correlation p-value. C) D492 and D492M cells treated with increasing concentrations of
795 the mTOR inhibitors everolimus and rapamycin. Results are presented as mean + standard error
796 (n≥4). D) Mechanism of glutathione synthesis inhibition by buthionine sulphoximine (BSO). GGC –
797 Gamma-L-glutamyl-L-cysteine. GCL – Glutamate-cysteine ligase, GSS – Glutathione synthetase. E)
798 Effect of 24-hour BSO-treatment on glutathione (GSH) concentration in D492 and D492M cells. F)
799 D492 and D492M cells treated with everolimus (0.005 μM) with and without BSO (50 μM). G) D492
800 and D492M cells treated with paclitaxel (0.005 μM) with and without BSO (50 μM). For F,G) the Y-
801 axis represents percentage of viability compared to non-treated cells after 72 hours of treatment
802 (mean + standard error, n≥4). Two-way analysis of variance (ANOVA) and Student's two-tailed t-test
803 (with Benjamini-Hochberg adjustment for multiple comparisons) were used to measure significance
804 of results in C) and E-G), respectively.

805

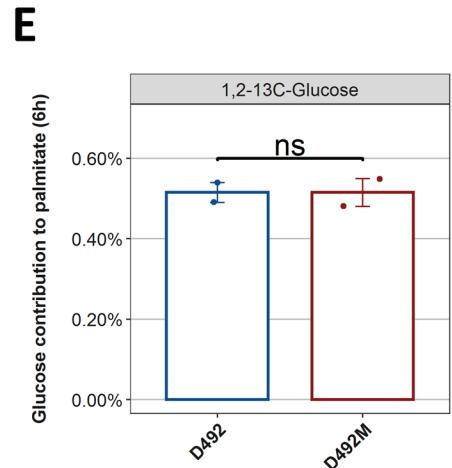
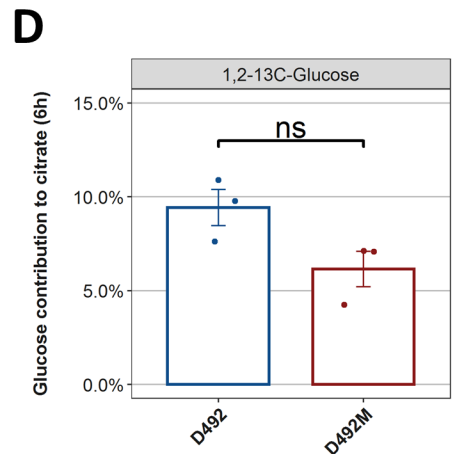
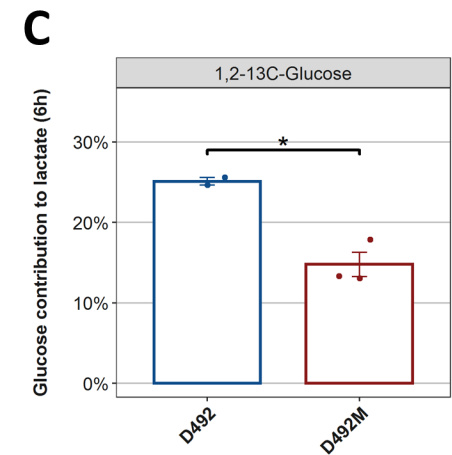
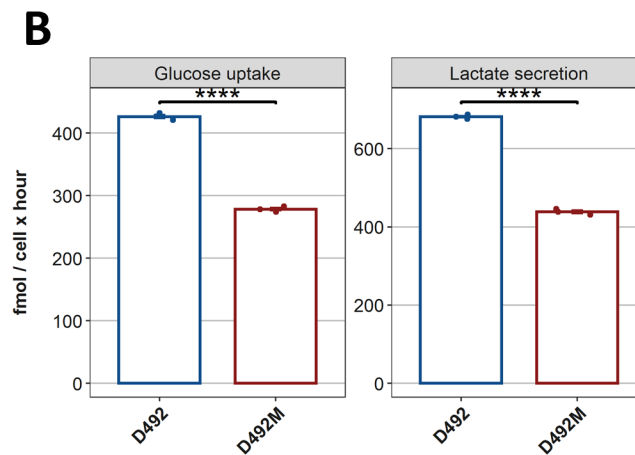
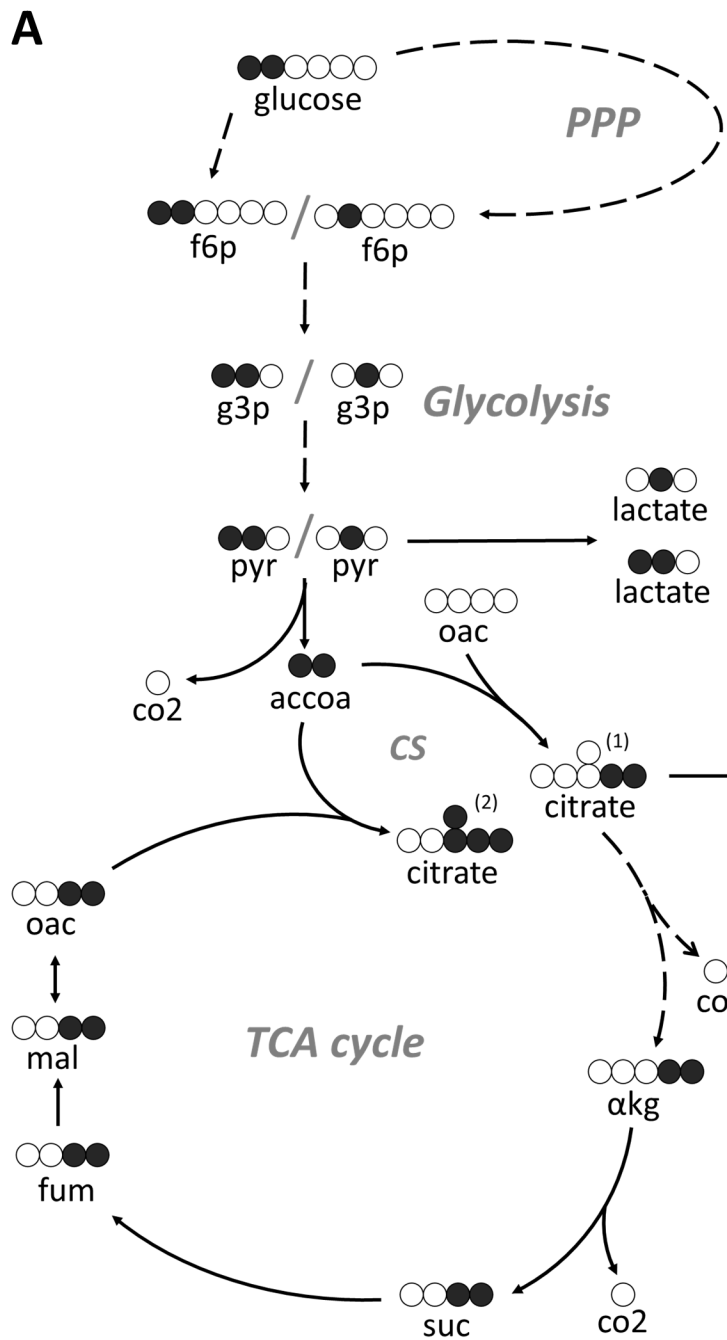


Figure 1

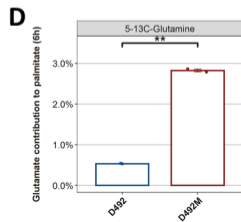
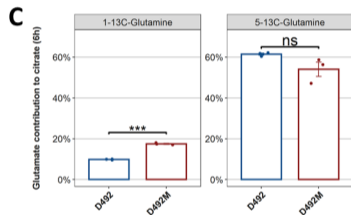
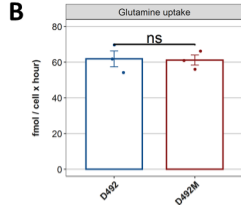
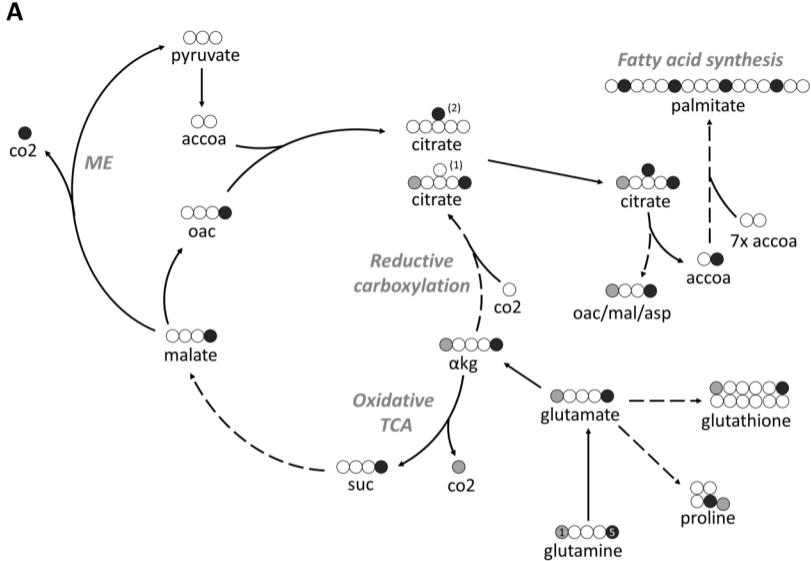


Figure 2

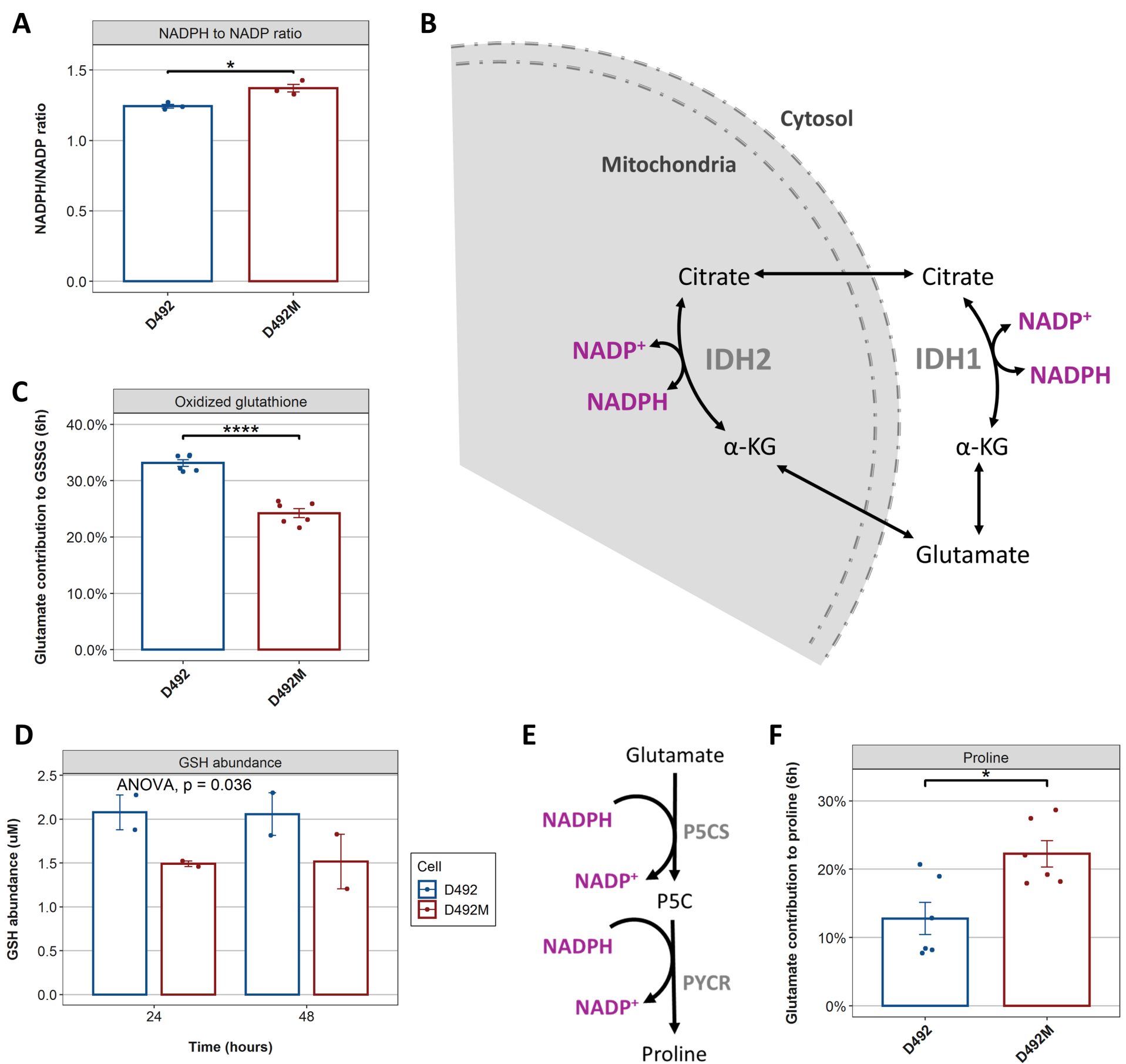


Figure 3

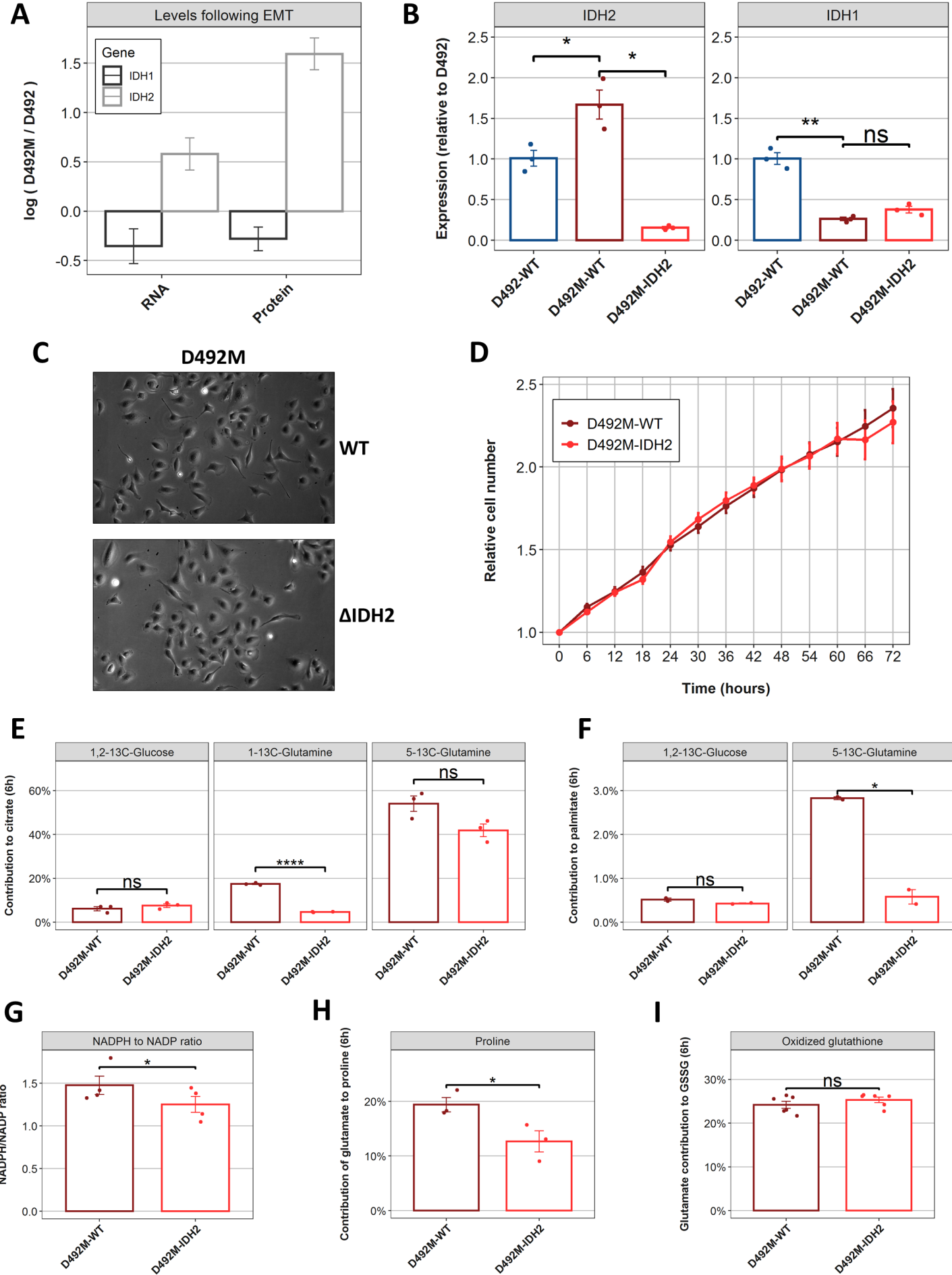


Figure 4

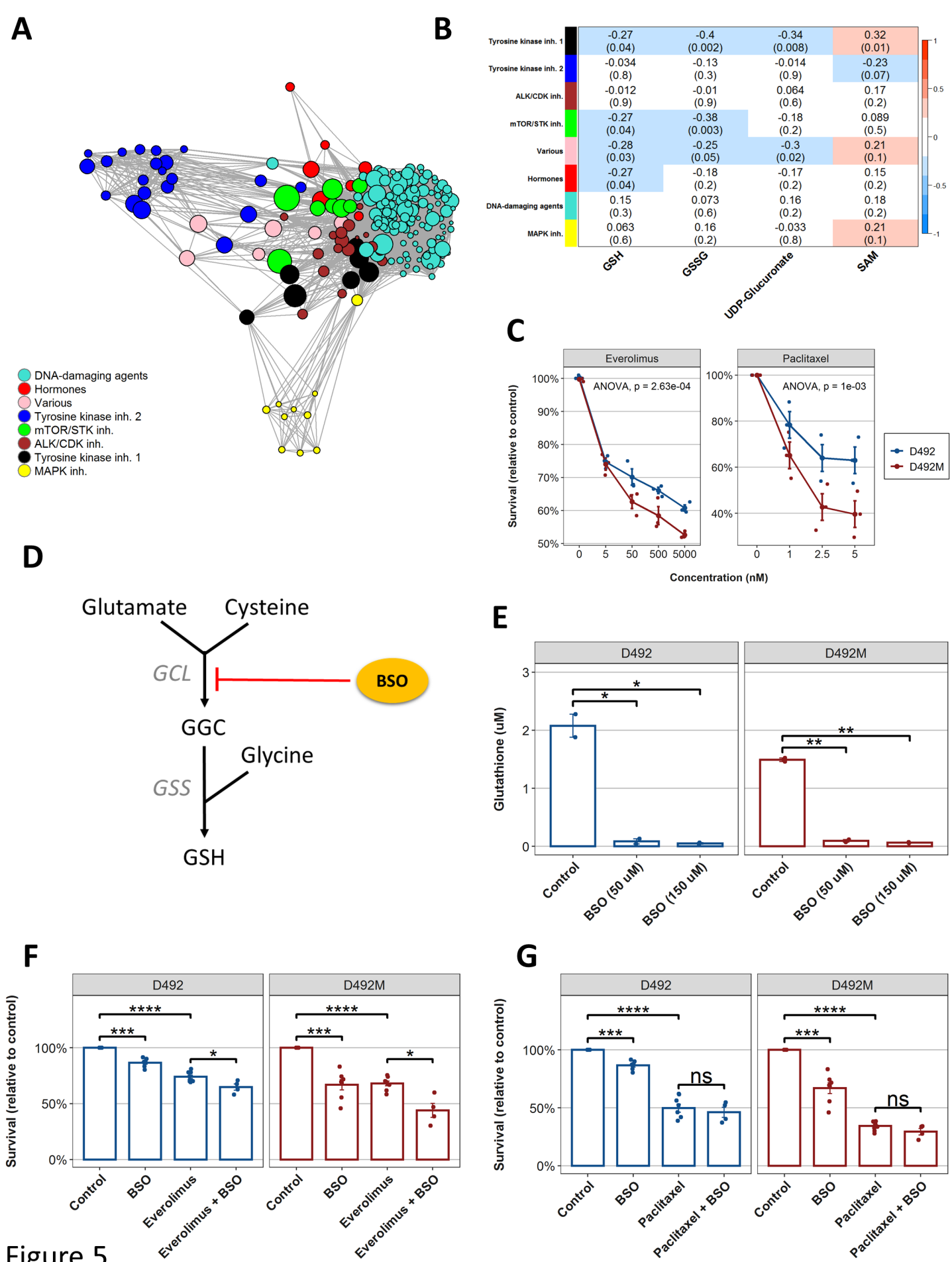


Figure 5